nature photonics

ARTICLES

https://doi.org/10.1038/s41566-022-00969-1

Check for updates

Chiral phonons in microcrystals and nanofibrils of biomolecules

Won Jin Choi[1,2,3], Keiichi Yano[2,3,4,12], Minjeong Cha[1,2], Felippe M. Colombari[5], Ji-Young Kim[2,3], Yichun Wang[2,3,7], Sang Hyun Lee[2,8], Kai Sun[1], John M. Kruger[9], André F. de Moura[10] ✉ and Nicholas A. Kotov[1,2,3,6,11] ✉

Chiral phonons are concerted mirror-symmetric movements of atomic groups connected by covalent and intermolecular bonds. Such lattice vibrations in crystals of biomolecules should be highly specific to their short- and long-range organizations, but their chiroptical signatures and structure–property relationships remain uncertain. Here we show that terahertz chiroptical spectroscopy enables the registration and attribution of chiral phonons for microscale and nanoscale crystals of amino acids and peptides. Theoretical analysis and computer simulations indicate that sharp mirror-symmetric bands observed for left- and right-handed enantiomers originate from the collective vibrations of biomolecules interconnected by hydrogen bonds into helical chains. The sensitivity of chiral phonons to minute structural changes can be used to identify physical and chemical differences in seemingly identical formulations of dipeptides used in health supplements. The generality of these findings is demonstrated by chiral phonons observed for amyloid nanofibrils of insulin. Their spectral signatures and polarization rotation strongly depend on their maturation stage, which opens a new door for medical applications of terahertz photonics.

Vibrations in simple crystal lattices, typically described as longitudinal and transverse phonons, commonly consist of parallel or perpendicular oscillatory displacements of atoms with respect to the propagation direction. As the complexity of the crystal lattice increases, the normal modes of phonons may become chiral due to the contribution of rotatory components. Besides their fundamental significance, chiral phonons favouring specific mirror-symmetrical left- and right-handed modes could be uniquely suitable for a wide range of emergent chiroptical technologies[1–3] including biomedical spectroscopy and photonics[4,5].

Two-dimensional materials, such as MoS_2 and WSe_2 (refs. [1,2]), may display chiral phonons; however, their hexagonal lattices are achiral. The left and right phonon modes coexist at the K/K′ point, resulting in a vanishing group velocity[6]. Chiral nanostructures[4] and crystals from non-centrosymmetric biomolecules (referred to as biocrystals for brevity) should break mirror symmetry for the left and right modes and enable the propagation of chiral phonons. Their propagation would be particularly interesting to observe for nanocrystalline fibrils of peptides known as amyloids because of their wide biological and biomedical significance. However, the phononic peaks are expected to be strongly broadened under conditions of nanoscale confinement[7].

In the early 2000s, strong vibrational modes attributed to phonons were observed for macroscale biocrystals of deoxyribonucleic acid, bovine serum albumin, collagen and benzoic acid[8–11]. These studies were facilitated by the rapid development of terahertz (THz) spectroscopy enabling measurements in photon energies ranging from 0.001 to 0.010 eV. Since then, a large number of studies have been carried out for crystals of amino acids (AAs), peptides, proteins and sugars[12–17]. Although some phonon resonances in the THz range were observed[16–20], the attribution of these peaks to specific lattice vibrations—chiral or not—was limited due to difficulties with the practical realization of terahertz circular dichroism (TCD) spectroscopy[21,22]. TCD would also be effective in resolving questions with peak attributions for the crystals of enantiomers and racemates that may have different space groups[13,20,23–25]. Additional fundamental questions of whether it is possible to distinguish biocrystals from L- and D-enantiomers or whether there are chiral phonons associated with specific mirror-symmetrical space groups remain open.

TCD spectra are expected to provide a unique analytical tool for probing chiral phonons in a wide range of molecular structures with direct relevance to chemical synthesis, biochemical quality control, protein folding and disease diagnostics[5,26–28]. There are also numerous applications of THz spectroscopy and imaging in medicine[29,30]: for nearly all of them, broad and featureless THz peaks are a detriment. TCD has the potential to resolve this problem by providing narrow bipolar peaks and easily quantifiable spectral features, such as null points[31]. In this perspective, TCD is analogous to electronic and vibrational circular dichroism spectroscopies but allows the evaluation of the mirror asymmetry of biocrystals, their space group and the normal modes of propagating phonons.

To identify chiral phonons, we measured the THz chiroptical properties of various biocrystals from AAs and dipeptides, later extending this method to amyloid nanofibrils. We chose the biocrystals of AAs as initial experimental and computational models because they are structurally versatile, serve as building blocks for

[1]Department of Materials Science and Engineering, University of Michigan, Ann Arbor, MI, USA. [2]Biointerfaces Institute, University of Michigan, Ann Arbor, MI, USA. [3]Department of Chemical Engineering, University of Michigan, Ann Arbor, MI, USA. [4]Department of Chemistry and Biotechnology, School of Engineering, The University of Tokyo, Tokyo, Japan. [5] Brazilian Biorenewables National Laboratory, Brazilian Center for Research in Energy and Materials, Campinas, Brazil. [6]Department of Biomedical Engineering, University of Michigan, Ann Arbor, MI, USA. [7]Department of Chemical and Biochemical Engineering, University of Notre Dame, South Bend, IN, USA. [8]Department of Electrical Engineering and Computer Science, University of Michigan, Ann Arbor, MI, USA. [9]Department of Small Animal Clinical Sciences, Michigan State University, East Lansing, MI, USA. [10]Department of Chemistry, Federal University of São Carlos, São Carlos, Brazil. [11]Program in Macromolecular Science and Engineering, University of Michigan, Ann Arbor, MI, USA. [12]Present address: Institute of Technology, Shimizu Corporation, Tokyo, Japan. ✉e-mail: moura@ufscar.br; kotov@umich.edu

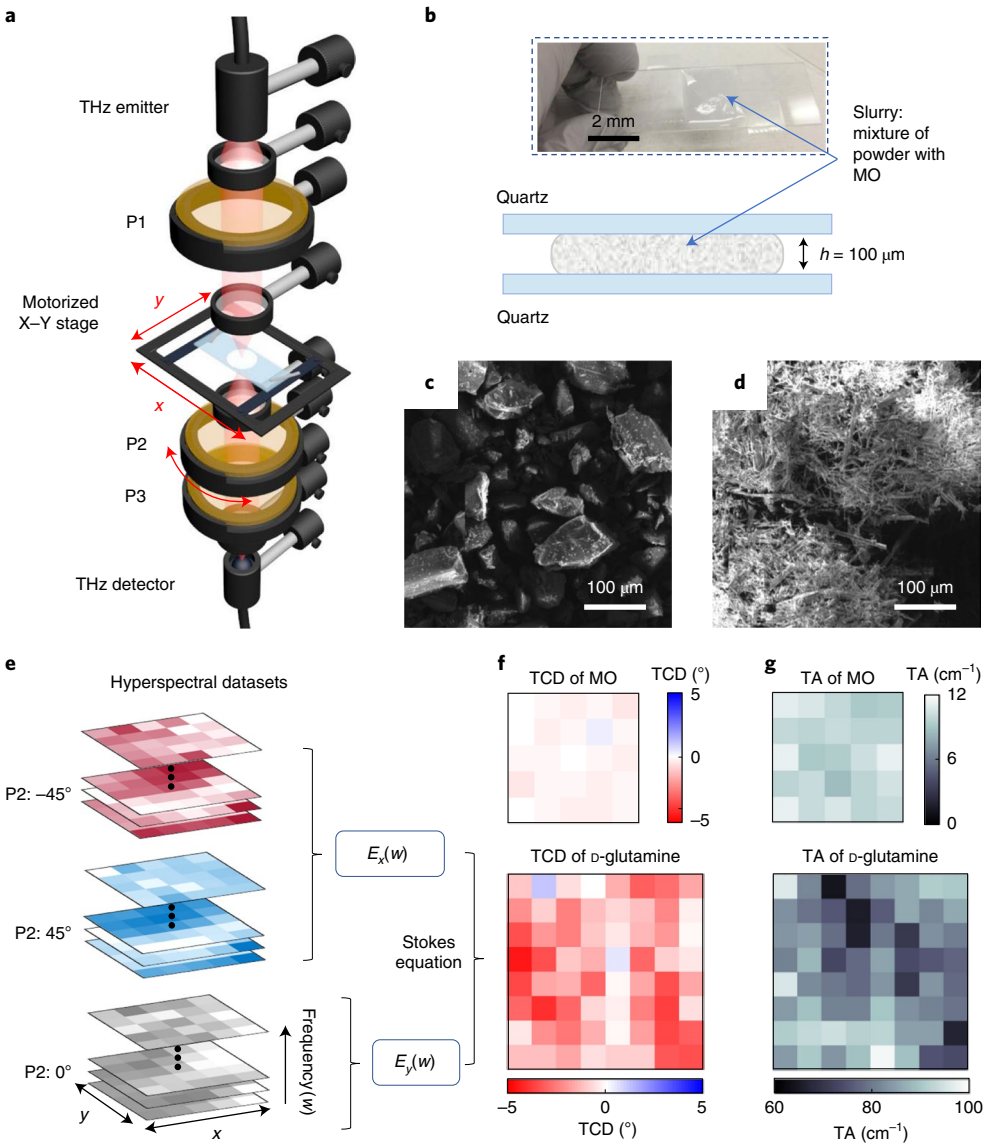

Fig. 1 | Hyperspectral THz-TDP setup for the observation of chiral phonons in AA microcrystals. a, Schematic of the THz-TDP setup. Three wire-grid polarizers (P1, P2 and P3) were used to analyse the polarization states of the beam after passing through the sample. A motorized X-Y stage was used for mapping. **b**, Photograph and schematic of the sandwich quartz cell with slurry mixtures. **c**,**d**, Scanning electron microscopy images before (**c**) and after (**d**) the recrystallization of L-glutamine. **e**, Fourier-transformed hyperspectral datasets of electric fields were measured by three different polarization measurements for each pixel. $E_x(w)$ is obtained from the measurements of 45° and -45° for the P2 polarizer and $E_y(w)$ is from 0°, which is along the *y* direction. **f**, Examples of TCD mapping for the reference MO and D-glutamine at 1.69 THz. **g**, Examples of TA mapping for reference MO and D-glutamine at 1.69 THz. The size of each pixel and the total scanning range in the images in **e**–**g** are 500 μm and 4 mm, respectively.

many biomolecules and are known to have strong absorption bands in the THz range[13,14,16,17]. Importantly, almost all AAs are available as left/right enantiomers, which makes them perfect enantiomorphic pairs of the chiral crystal space group. Also, computational difficulties related to the calculations of chiral phonons can be accurately and efficiently addressed with the recently developed semiempirical GFN2-xTB Hamiltonian[32].

One of the roadblocks on this path is that the implementation of chiroptical spectroscopy methods in the THz range is far from trivial, especially for biological materials[21,22]. Standard THz absorption (TA) experiments showed strong dependence of the TA spectra on sample preparation, which can only be exacerbated for TCD due to large contributions of linear dichroism and circular birefringence[33]. Seemingly minor presence of the opposite enantiomer of AA and impurities can also distort or change their crystal habits[12,27], resulting in spectral distortions and peak broadening (Supplementary Discussion and Supplementary Fig. 5). Since AAs can have multiple crystalline phases and hydration states, their careful verification by powder X-ray diffraction (PXRD) analysis is also required.

To address these problems, we utilized a terahertz time-domain polarimetry (THz-TDP) setup with motorized X–Y scanning (Fig. 1a). This enables the accurate measurements and identification of chiral phonons by acquiring statistically averaged TA, TCD and terahertz optical rotary dispersion (TORD) spectra (Fig. 1e–g). To acquire reliable chiroptical spectra, we used concentrated slurries containing 50 wt% recrystallized AA crystals (dimensions, <20 μm) in mineral oil (MO). The random orientation of densely packed microcrystals in slurries eliminates the problems typically observed in pressured and pelleted samples with linear dichroic effects and powder samples with electrostatic charges (Fig. 1b–d

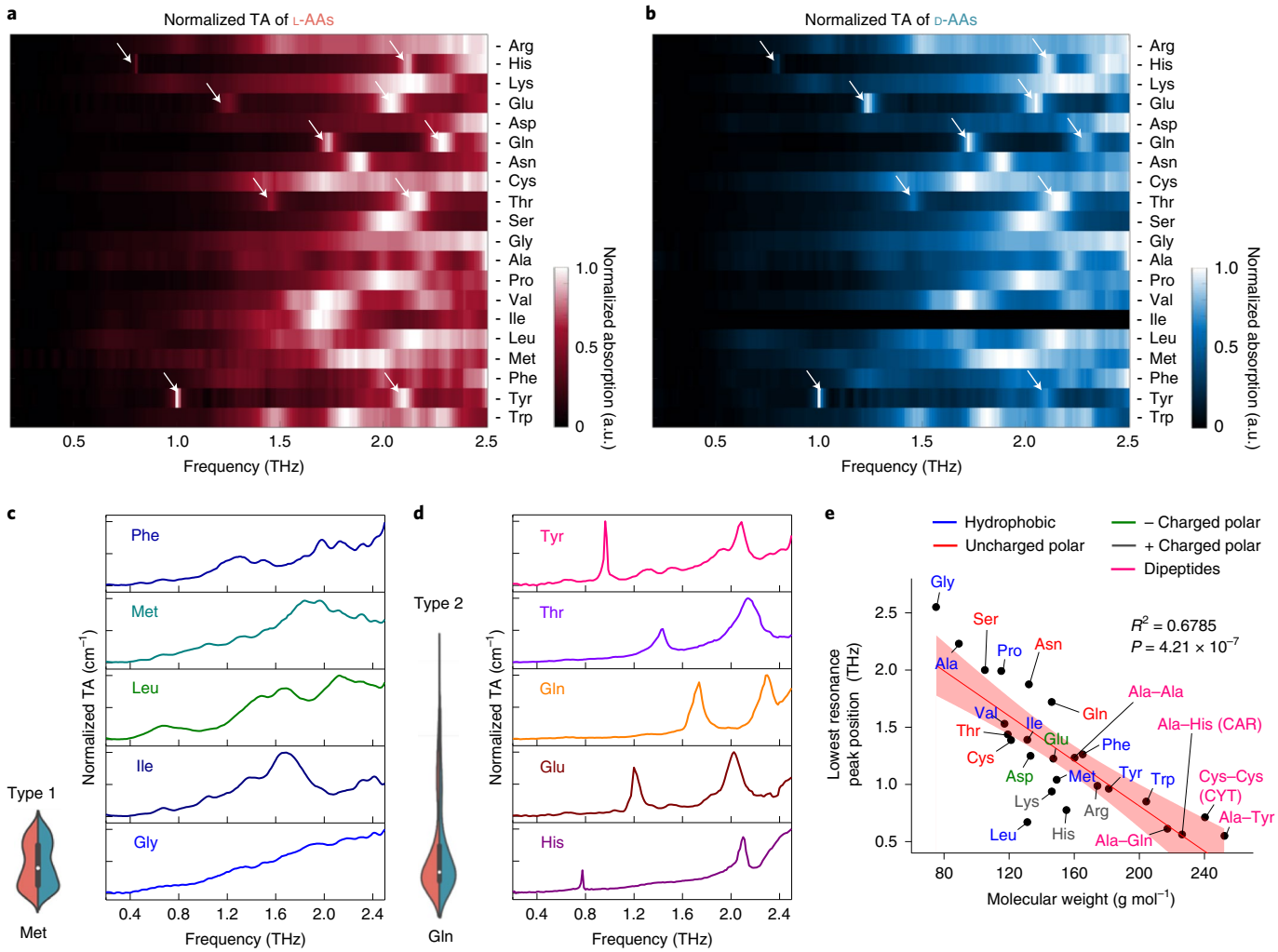

Fig. 2 | Analysis of TA spectra for L- and D-enantiomers of 20 AAs. a,**b**, Two-dimensional plot of the TA spectra of L-AAs (**a**) and D-AAs (**b**) with band intensity represented by colour brightness. The same samples of achiral glycine were used for the TA analysis. The white arrows indicate the appearance of sharp peaks in the spectra. **c**,**d**, Normalized TA spectra of five representative L-AAs having broad peaks (**c**) and sharp peaks (**d**). The shape of the distribution is dependent on the width of the peaks: broad-peak AAs, type 1; sharp-peak AAs, type 2. Data in **c** and **d** are presented as mean values ± s.d. **e**, Molecular-weight dependence of the lowest THz resonance peak position. The lowest peak appearing above the baseline was chosen for each AA crystal and the exact peak positions of the absorption peaks are summarized in Supplementary Table 4. AAs with larger molecular mass show lower resonance frequencies. The mean frequencies of AAs (red solid line) and their s.d. values (red shading; 95% confidence interval). *R*-squared and *P* values are analysed by the *t*-test (d.f. = 23), one sided and with no adjustment.

and Supplementary Discussion). Similar problems and mitigations are typical of electronic circular dichroism measurements in the visible range[34]. A quartz sandwich cell with a 100 µm spacer maintaining the uniformity of the optical wavefront and thin, constant sample thickness was utilized to obtain high signal-to-noise ratios. The TA for each pixel was directly calculated from E_x and E_y, the electric fields in the x and y directions, respectively, and fast Fourier transformation of the electric fields in the x and y directions obtained by three different polarization measurements, whereas the TCD and TORD spectra for each pixel were determined from the Stokes equations (Fig. 1e–g and Supplementary Information)[21].

The TA spectra of the 20 AAs obtained in this study (Fig. 2a,b) as well as the TA spectra observed for their subset using pelleted samples in prior studies[13,14,16] consistently indicate that L- and D-enantiomers show almost identical TA spectra. Two dominant types of TA spectrum can be easily recognized for all the AAs (Fig. 2a–d). Type 1 spectra, exemplified by methionine (Met), show monotonically increasing absorptions with broad peaks, whereas type 2 spectra, exemplified by glutamine (Gln) or glutamic acid (Glu), display multiple sharp peaks. Their visual identification and classification can be confirmed by a dynamic time-warping algorithm and statistical spectrum density plots ('violin' plots) (Supplementary Fig. 18). Going further, we found that type 1 and type 2 spectra nearly correlate perfectly with the symmetry group of the unit cell of the AA crystals (Supplementary Table 2). Note that neither type 1 nor type 2 groups correlate with the chemical properties of the side chains (Supplementary Fig. 18). Rather, a negative correlation with the molecular masses of AAs was observed (Fig. 2e and Supplementary Table 4), indicating that the collective long-range displacements of an entire molecule is coupled to these vibrational modes[35].

All five type 2 AAs crystallize in the orthorhombic space group $P2_12_12_1$ (Fig. 2d)—the most common space group for biocrystals[36]. Type 1 AAs crystallize in the monoclinic space groups $P2_1$ or $C2$ (Fig. 2c). The sharp peaks in the spectra of type 2 AAs were investigated in greater detail. The $P2_12_12_1$ space group has three 2_1 screw

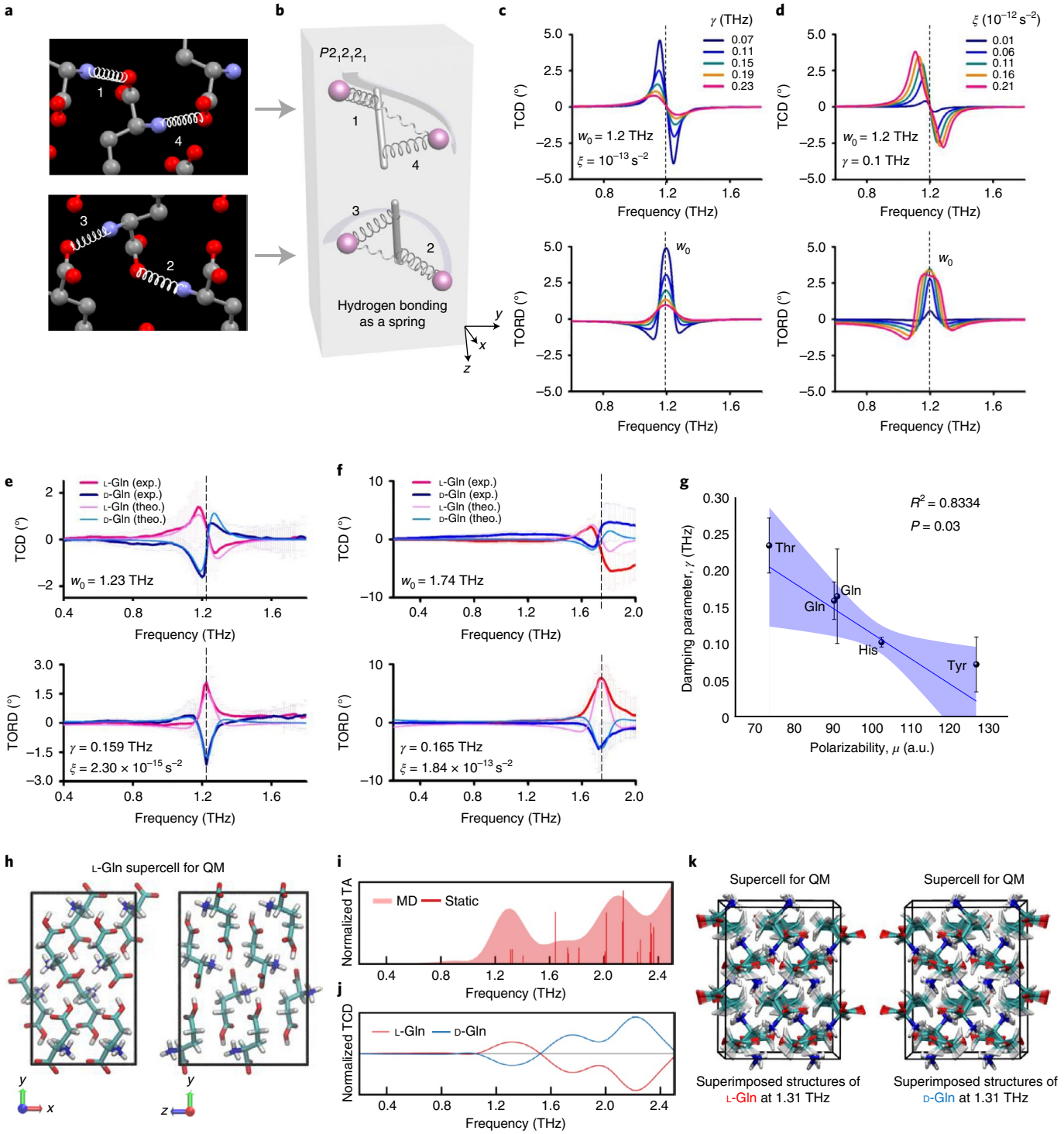

Fig. 3 | Analysis of TCD and TORD spectra for L- and D-enantiomers of 20 AAs. a, Enlarged view of hydrogen bonds in L-Glu crystal cell as an example of a compound crystallizing in the $P2_12_12_1$ space group. Amino groups are helically arranged in the 1–2–3–4 progression. Hydrogen bonds represented as springs in the BK model used for a heuristic description of chiral phonons. **b**, Schematic of the unit cell with bi-oscillators in the $P2_12_12_1$ space symmetry. **c**,**d**, TCD and TORD data calculated from the BK model by varying the damping parameter γ (**c**) and coupling strength ξ (**d**). **e**,**f**, Experimental (exp.) and calculated (theo.) TCD and TORD spectra of Glu (**e**) and Gln (**f**). **g**, Dependence of γ on polarizability μ of AA molecules[39,40]. The data in **g** are presented as mean values ± s.d. The mean damping parameters of AAs (blue solid line) and their s.d. values (blue shading; 95% confidence interval). *R*-squared and *P* values are analysed by the *t*-test (d.f. = 3), one sided and with no adjustment. **h**, Supercell of L-Glu used for the QM computations of the THz spectra. **i**, Normalized TA spectra obtained from the calculations of the L-Glu supercell in **h** using the normal-mode analysis (vertical lines) and MD simulations at the QM level (solid surfaces). **j**, Normalized TCD spectra from the same MD simulations at the QM level used for TA in **i**. **k**, Superimposed structures of the L-Glu molecules along the normal mode (eigenmode) with a frequency of 1.31 THz for the system depicted in **h** (left) and its mirror image (right).

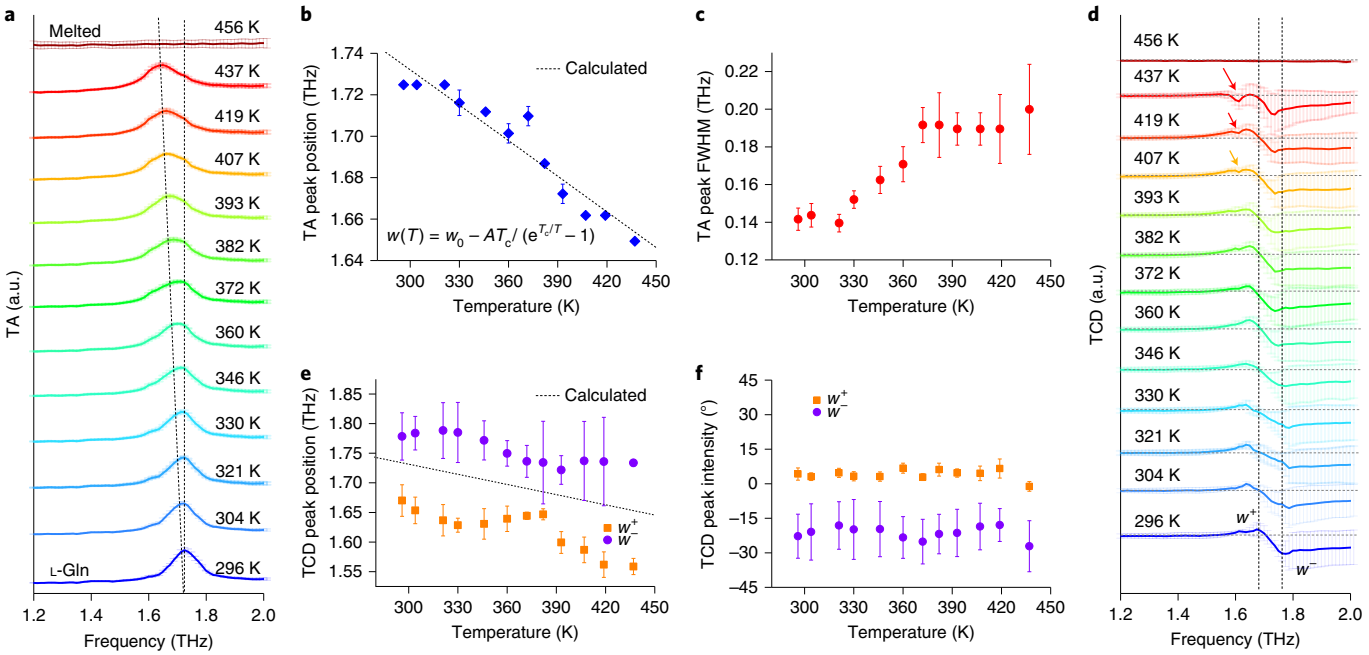

Fig. 4 | Temperature dependence of TA and TCD spectra for L- and D-glutamine. a, TA spectra of L-Gln at temperatures from 296 to 456 K. For clarity, only the spectral data in the 1.2–2.0 THz range are shown. The spectra are vertically offset and the dotted lines are guides to the eye. **b**, Phonon-mode softening on temperature increase and the dotted line is a fit by a Bose–Einstein distribution. The fitting parameters are $w_0 = 1.86$ THz, $A = 5.8 \times 10^{-4}$ THz K^{-1} and $T_c = 152$ K. **c**, Change in the peak width (full-width at half-maximum (FWHM)). **d**, Evolution of the chiral phonon modes of L-Gln in the same temperature range. **e**,**f**, Temperature dependence of the position (**e**) and intensity (**f**) of the TCD peak. The dotted line in **e** is a fit by the Bose–Einstein distribution. The circles indicate the positions of positive peaks (w^+) and squares are those of negative peaks (w^-) in **d**. The data in **b**,**c**,**e** and **f** are presented as mean values ± s.d.

axes producing chiral patterns inside the unit cell. Correspondingly, the nitrogen atoms of the amino groups (–NH_2) and N–H···O hydrogen bonds form helices in the unit cell (for example, L-Glu; Supplementary Fig. 20). To investigate the mirror asymmetry of the observed phononic modes, the TCD spectra of AAs and their enantiomers were obtained (Supplementary Fig. 17). All five type 2 AAs (histidine (His), Glu, Gln, threonine (Thr) and tyrosine (Tyr)) forming crystals in the $P2_12_12_1$ space group showed distinct bisignate TCD peaks at a low frequency, with nearly perfect mirror symmetry for L- and D-enantiomers, clearly indicating the chirality of these phonons (Supplementary Fig. 22). For comparison, no TCD spectra could be registered in the achiral crystals of caesium iodide (CsI) despite an exceptionally strong phonon mode at 1.84 THz (Supplementary Fig. 16)[37]. Other AAs may also support some modes of chiral phonons but their TCD spectra are broad, which are probably the result of the superposition of multiple overlapping modes (Supplementary Fig. 17).

The Born–Kuhn (BK) model of coupled bi-oscillators[38] may provide an approximate heuristic level of understanding of chiral phonons in various biocrystals including nanofibrils. Unlike previous versions of the BK model used for chiral plasmons[38], the bi-oscillators shown in Fig. 3a,b represent AA segments coupled via hydrogen bonds. They are stacked on top of each other with twists between the molecules, similar to the $P2_12_12_1$ lattice (Supplementary Fig. 20c). A left- or right-circularly polarized beam matching the handedness of the bi-oscillators can thereby excite their collective vibrations (Fig. 3b). The polarization-dependent light absorption is represented by the non-locality tensor, $\mathbf{\Gamma}(k, w)$; for the model shown in Fig. 3c,d, it acquires the following form:

$$\mathbf{\Gamma}(k, w) = \frac{DN_0e^2}{3m} \frac{\xi}{(w_0^2 - i\gamma w - w^2)^2 - \xi^2}, \quad (1)$$

where w_0 is the resonance frequency, γ is the damping parameter, ξ is the coupling strength between the two oscillators and m is mass of the individual oscillator; the remaining constants and variables are defined in the Supplementary Information. The inverse dependence of $\mathbf{\Gamma}(k, w)$ on m (equation (1)) rationalizes the empirically observed inverse relationship between the position of the TA peak and molecular mass of AAs (Fig. 2e). The TCD and TORD spectra can be calculated from $\mathbf{\Gamma}(k, w)$ by applying the Drude–Born–Fedorov formalism[38] as

$$\mathrm{TCD} = \frac{2w}{c} \mathrm{Im}\{\mathbf{\Gamma}\}, \quad (2)$$

$$\mathrm{TORD} = \frac{w}{2c} \mathrm{Re}\{\mathbf{\Gamma}\}, \quad (3)$$

where c and w are the speed of light and oscillation frequency, respectively (Supplementary Information). The calculated TCD and TORD spectra are well matched to the shape and position of the experimentally obtained values (Fig. 3e,f and Supplementary Fig. 22). As perhaps expected, increases in the coupling parameter ξ increase the amplitude of the TCD and TORD peaks, which shows that stronger intermolecular bonds in biocrystals promote the propagation of chiral phonons (Fig. 3d). Concurrently, an increase in damping parameter γ reduces the intensity of the chiroptical THz peaks (Fig. 3c). Since both ξ and γ strongly influence the shapes of the TCD and particularly the TORD peak, one can confidently fit the experimental data with the BK model, obtaining the values of γ and ξ (Supplementary Table 5) for several type 2 AAs (Fig. 3e,f and Supplementary Fig. 22). We also found an inverse relation between γ and polarizability μ for the biocrystals of AAs (Fig. 3g), which facilitates the selection of biocrystals predisposed to high-intensity chiral phonons (Supplementary Fig. 21)[39,40].

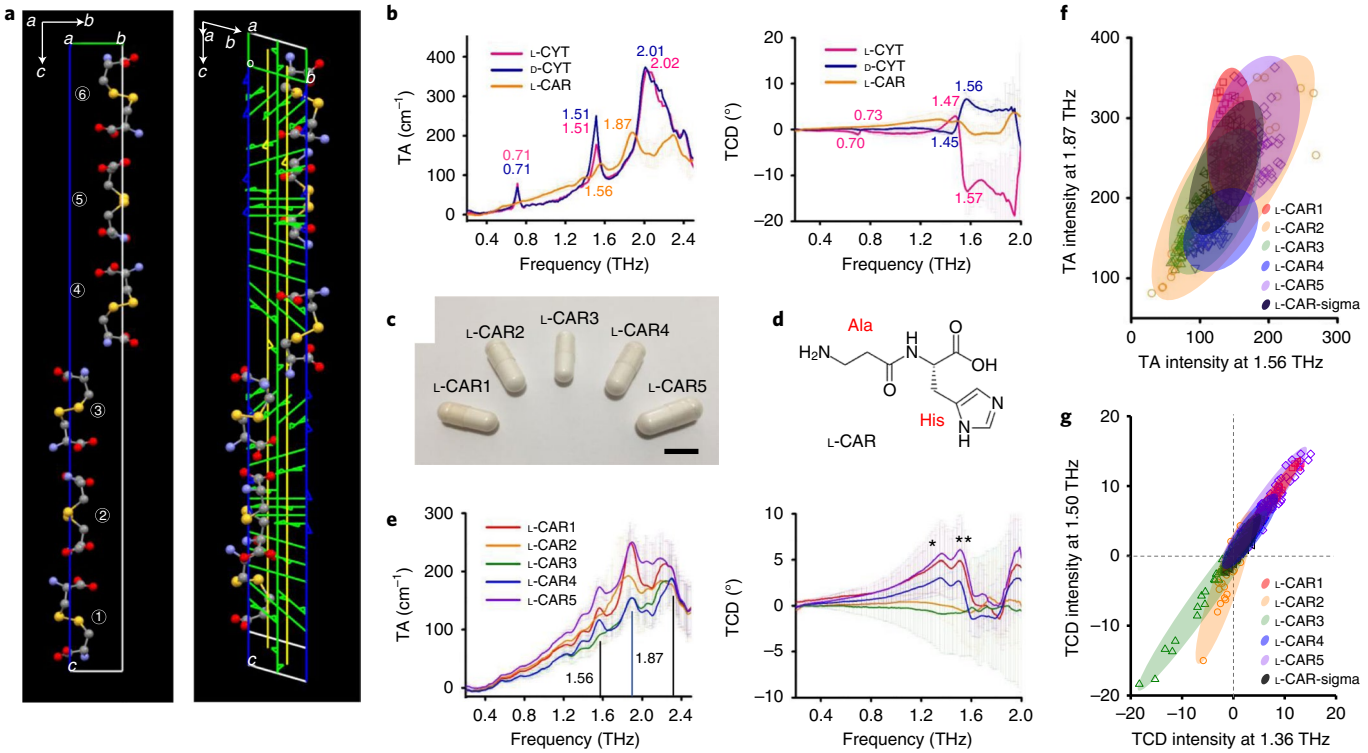

Fig. 5 | Chiral phonons in CYS and CAR. a, Helical axes of L-CYT molecules in a unit cell. Six L-CYT molecules winding a 6_1 screw axis that coincides with the *c* axis (indicated by the green helical 'scaffold'). **b**, Averaged TA and TCD spectra from L-CYT, D-CYT and L-CAR. **c**, Photograph of five different pills from various manufacturers used for measurements. Scale bar, 1 cm. **d**, Molecular structure of L-CAR dipeptide. **e**, Average TA and TCD spectra from as-received L-CAR from five different manufacturers. The * and ** indicate the first and second peak positions of TCD at 1.33 THz and 1.51 THz, respectively. **f**,**g**, Two-dimensional peak intensity distribution map of TA (**f**) and TCD (**g**) from as-received L-CAR samples.

Further insights into the nature of lattice vibrations in AA crystals were obtained from atomistic computer simulations. A periodic supercell containing $2 \times 1 \times 2$ unit cells of L-Glu was used for calculations of the phonon normal modes at the quantum-mechanical (QM) level using the GFN2-xTB Hamiltonian[32] (Fig. 3h) implemented in the CP2K program[41] (Supplementary Information). The calculated TA (Fig. 3i) and TCD (Fig. 3j) spectra agree very well with the experimental results (Figs. 2d and 3e). We were also able to identify the actual chiral phonon modes responsible for the appearance of peaks in the TCD spectra. As such, the normal mode for the 1.2–1.4 THz peak in the crystals of L-Glu involves the twisting of the carboxylate groups from both main chain and side chain with dihedral angles changing by tens of degrees (Fig. 3k, Supplementary Information and Supplementary Video 2). The handedness of the rotatory motion of these groups is opposite for the two Glu enantiomers (Fig. 3k). The broad peaks observed for type 1 AAs represent the superposition of several normal modes, as exemplified for the lattice vibrations observed for L-Met (Supplementary Fig. 27 and Supplementary Video 2). A comparison of the crystallographically derived structures of the AAs show the structural differences between the two types of AA crystal. In type 1 AAs, the side chains mostly interact via van der Waals forces, whereas the main chains are strongly bound by ionic interactions between the charged groups. In contrast, charged or polar groups of the side chains of type 2 AAs allow the formation of a homogeneous and strong network of supramolecular bonds throughout the crystal, which leads to the emergence of sharp TA, TCD and TORD peaks as spectroscopic signatures of chiral phonons; this concurs with the high values of coupling parameter ξ established using the BK model. Besides its importance in rationalizing the TA and TCD results, this structure–property relationship opens the possibility to 'tune' the chiral phonon frequencies in engineered synthetic crystals.

An analysis of the temperature dependencies of the TA and TCD spectra can further shed light on the nature of the observed THz peaks (Fig. 4). Phonon modes generally undergo broadening and a redshift at elevated temperatures, which can be clearly observed for L-Gln (Fig. 4a). Since phonons are bosons, the temperature dependence is expected to follow the Bose–Einstein statistics, which has been verified (Fig. 4b). Notably, the pre-exponent $A = 5.8 \times 10^{-4}\,\mathrm{THz\,K^{-1}}$ and the characteristic temperature of chiral phonons $T_c = 152\,\mathrm{K}$ in Gln are fairly similar to those observed for purine and adenine[42], pointing to the similarity of the energy of the hydrogen-bonded network in their crystals. The 'softening' of phonons can also be seen from the temperature-dependent TCD spectra (Fig. 4d,e). However, the TCD spectra also show an additional peak emerging above 407 K (Fig. 4d, arrow), which is different from any temperature dependencies on phonons observed before[12,42,43] or the formation of Bose–Einstein condensates of phonons observed for decreased temperatures in WS_2 nanosheets[44] or protein crystals[45]. The rise of the new peak indicates the gradual increase in complexity of the phononic mode at elevated temperatures to include additional mirror-symmetric motions exemplified by segmental twisting.

The temperature points to the fact that the concerted movement of molecules characteristic for chiral phonons (Supplementary Video 2) makes them highly sensitive to both short- and long-range organization of molecular lattices. To further investigate this point and to demonstrate the generality of chiral phonons, the TA, TCD and TORD spectra of dipeptides, including Ala–Ala, Ala–Tyr, Ala–Gln, Gly–Gly, cystine (Cys–Cys linked via disulfide (S–S) bonds, CYT) and carnosine (Ala–His, CAR) were acquired

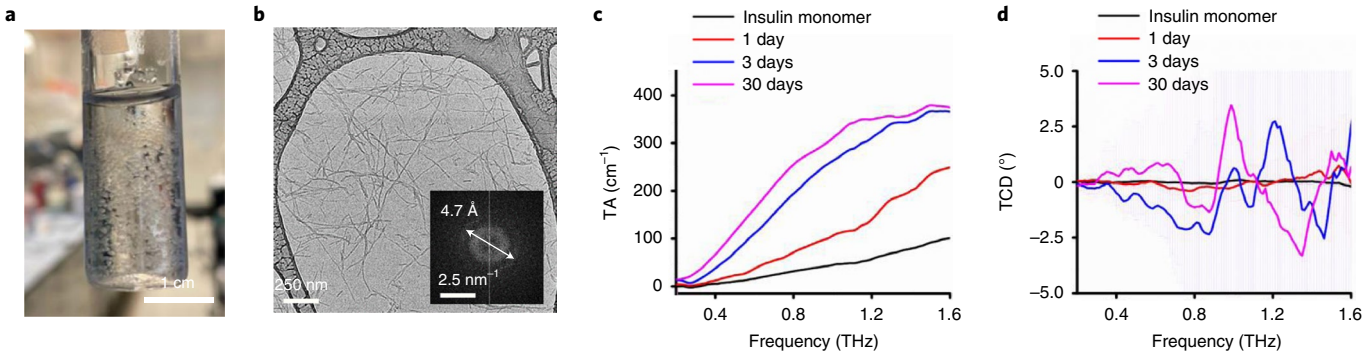

Fig. 6 | Formation of amyloid fibrils of insulin and their TA and TCD spectra. a, Photograph of insoluble insulin fibrils formed at pH 2. **b**, TEM image of insulin fibrils. The inset shows the selected-area electron diffraction pattern corresponding to a bundle of insulin fibrils. The reflection at 4.7 Å corresponds to the separation of strands within each β-sheet. There are also weak reflections between 9.0 and 12 Å. **c**,**d**, Averaged TA (**c**) and TCD (**d**) spectra of insulin from monomers to 30 days of fibrillation. The data in **c** and **d** are presented as mean values ± s.d.

(Fig. 5 and Supplementary Fig. 25). Note that L-CYT is the key component of kidney and bladder stones[46], whereas L-CAR is a nutritional supplement, which prompted us to investigate them in greater detail.

Here L-CYT crystallizes as hexagonal plates ($P6_122$ chiral space group, $a=b=0.54$ nm, $c=5.60$ nm) and the six CYT molecules in the unit cell are helically organized about the 6_1 screw axis (Fig. 5a)[46]. Similar to type 2 AAs, the TA spectra of L- and D-CYT show sharp peaks in the spectral window between 0.2 and 2.5 THz (Fig. 5b). The lowest resonance peak positions at 0.71 and 0.56 THz (Fig. 2g) agree well with the molecular weight of CYT (240.30 g mol^{-1}) and CAR (226.23 g mol^{-1}), respectively. The TCD spectra of CYT enantiomers display mirror-symmetrical peaks (Fig. 5b), with the most intense TCD peak at 1.57 THz matching very well with the TCD predictions from simulations of the CYT supercell (Supplementary Fig. 28 and Supplementary Videos 1 and 2). In addition, the attribution of both bands to chiral phonons was confirmed by the spectroscopic data for DL-CYT and deuterated L-CYT (Supplementary Fig. 23). The spectral signatures of L-CYT were also identified in the samples of canine bladder stones (Supplementary Fig. 24).

The variability of chiral phonon signatures from L-CAR was also tested in seemingly identical health supplements from five different manufacturers (Fig. 5c,d). The TA and TCD spectra (Fig. 5e) show large differences between these L-CAR formulations. Ideally, the intensities of TA and TCD peaks should have the same ratio in all the products and minimal sample-to-sample variations. However, this was not the case, as can be visualized by the TA and TCD distribution maps (Fig. 5f,g). These maps show distinct peak correlations specific to each manufacturer, which can be associated with structural differences in the crystallinity of and impurities in the specific L-CAR formulations. The high sensitivity of non-locality tensor $\boldsymbol{\Gamma}(k,w)$ to parameter ξ in the BK model indicates that factors such as environmental and thermal aging of biocrystals[47], which affect the strength of hydrogen bond 'springs', must affect their TCD spectrum. Indeed, the changes in the TA and TCD spectra of L-CAR samples after heating at 65 °C for two days (Supplementary Fig. 29) clearly show dramatic changes in the chemical and physical states of these health supplements. The displacement and broadening of TCD peaks are also specific to each manufacturer, presumably due to various chiral and achiral additives.

Following the structure–property relationships identified above and the progression of experimental data from single AA to dipeptides, one may also expect that assemblies of peptides may support the propagation of chiral phonons, too. Some of the most important ones are nanofibrils of amyloid peptides. These crystalline fibres are strongly interconnected by hydrogen bonds and intermolecular hydrophobic attractions. The observation of chiral phonons in the nanofibrils of amyloids also highlights the significance of TCD for biomedical applications because amyloid fibrillation—the process of soluble proteins misfolding into insoluble fibrils comprising α-helices and/or β-sheets—is an important clinical hallmark of various health disorders from skin cancer and Alzheimer's disease to type 2 diabetes[48].

We measured the TA and TCD spectra of amyloid fibrils of insulin (Fig. 6a) with a diameter of around 10 nm as visualized by transmission electron microscopy (TEM; Fig. 6b). Insulin nanofibrils are known to undergo structural changes from a predominantly α-helix to β-sheet conformation[49] during fibrillation. Indeed, a strong reflection at 4.7 Å—corresponding to the distance between the peptide strands in the β-sheets—was observed by electron diffraction (Fig. 6b, inset)[49]. Chiral phonon modes of insulin nanofibrils were identified by TCD (Fig. 6d), and distinctive positive and negative peaks showed higher spectral resolution than the broad TA spectra (Fig. 6c). Note that the intensity of TCD spectra dramatically increases as insulin assembles into fibrils, which is fully consistent with the expected emergence of chiral phonons despite the potential broadening[7]. The sign of the TCD peak at 1.2 THz reverses from positive to negative with the maturation of nanofibres, which is consistent with the change from right-handed helicity in the α-helix to left-handed helicity in β-sheets[50].

In conclusion, the identification of chiral phonons in the THz range in microcrystals and nanofibrils of biomolecules, as well as the elaboration of a spectroscopic toolbox for them, opens the door to a large family of materials where the complex collective vibrations of crystal lattices with rotatory components can be investigated. Due to the strong sensitivity of chiral phonons to the chemical interactions in the crystal lattice, the spectroscopic methodology of circular dichroism in the THz range can be used to (1) observe variations in phonon modes with temperature and (2) carry out quality control testing in the biomedical industry[26,27]. The existence of narrow TCD lines for chiral phonons also enables their further investigation for biomedical imaging[30] and chiral photonics. Non-invasive and label-free toolbox of TCD may play a significant role in monitoring insulin fibrillation for in vivo and ex vivo conditions. The library of THz fingerprints from basic AAs to complex proteins and other biomolecular complexes opens a new horizon for THz bioinformatics and deepens our understanding of many collective-vibration-mediated (bio) chemical processes and multiscale chirality of self-assembled biological nanostructures.

Online content

Any methods, additional references, Nature Research reporting summaries, source data, extended data, supplementary information, acknowledgements, peer review information; details of author contributions and competing interests; and statements of data and code availability are available at https://doi.org/10.1038/s41566-022-00969-1.

Received: 16 February 2021; Accepted: 30 January 2022;
Published online: 21 March 2022

References

1. Zhu, H. et al. Observation of chiral phonons. *Science* **359**, 579–582 (2018).
2. Yuan, X. et al. The discovery of dynamic chiral anomaly in a Weyl semimetal NbAs. *Nat. Commun.* **11**, 1259 (2020).
3. Yeom, J. et al. Chiromagnetic nanoparticles and gels. *Science* **359**, 309–314 (2018).
4. Kurouski, D. Advances of vibrational circular dichroism (VCD) in bioanalytical chemistry. A review. *Anal. Chim. Acta* **990**, 54–66 (2017).
5. Keiderling, T. A. Protein and peptide secondary structure and conformational determination with vibrational circular dichroism. *Curr. Opin. Chem. Biol.* **6**, 682–688 (2002).
6. Chen, H., Wu, W., Zhu, J., Yang, S. A. & Zhang, L. Propagating chiral phonons in three-dimensional materials. *Nano Lett.* **21**, 3060–3065 (2021).
7. Adu, K. W., Gutiérrez, H. R., Kim, U. J., Sumanasekera, G. U. & Eklund, P. C. Confined phonons in Si nanowires. *Nano Lett.* **5**, 409–414 (2005).
8. Markelz, A. G., Roitberg, A. & Heilweil, E. J. Pulsed terahertz spectroscopy of DNA, bovine serum albumin and collagen between 0.1 and 2.0 THz. *Chem. Phys. Lett.* **320**, 42–48 (2000).
9. Markelz, A., Whitmire, S., Hillebrecht, J. & Birge, R. THz time domain spectroscopy of biomolecular conformational modes. *Phys. Med. Biol.* **47**, 3797–3805 (2002).
10. Walther, M., Plochocka, P., Fischer, B., Helm, H. & Uhd Jepsen, P. Collective vibrational modes in biological molecules investigated by terahertz time-domain spectroscopy. *Biopolymers* **67**, 310–313 (2002).
11. Fischer, B., Walther, M. & Jepsen, P. U. Far-infrared spectroscopy of hydrogen bonding in nucleobases, nucleosides, and nucleotides. In *Proc. IEEE Tenth International Conference on Terahertz Electronics* 74–76 (IEEE, 2002).
12. Walther, M., Fischer, B. M. & Jepsen, P. U. Noncovalent intermolecular forces in polycrystalline and amorphous saccharides in the far infrared. *Chem. Phys.* **288**, 261–268 (2003).
13. Williams, M. R. C., Aschaffenburg, D. J., Ofori-Okai, B. K. & Schmuttenmaer, C. A. Intermolecular vibrations in hydrophobic amino acid crystals: experiments and calculations. *J. Phys. Chem. B* **117**, 10444–10461 (2013).
14. Rungsawang, R., Ueno, Y., Tomita, I. & Ajito, K. Angle-dependent terahertz time-domain spectroscopy of amino acid single crystals. *J. Phys. Chem. B* **110**, 21259–21263 (2006).
15. Neu, J. et al. Terahertz spectroscopy of tetrameric peptides. *J. Phys. Chem. Lett.* **10**, 2624–2628 (2019).
16. Korter, T. M. et al. Terahertz spectroscopy of solid serine and cysteine. *Chem. Phys. Lett.* **418**, 65–70 (2006).
17. Singh, R., George, D. K., Benedict, J. B., Korter, T. M. & Markelz, A. G. Improved mode assignment for molecular crystals through anisotropic terahertz spectroscopy. *J. Phys. Chem. A* **116**, 10359–10364 (2012).
18. Korter, T. M. & Plusquellic, D. F. Continuous-wave terahertz spectroscopy of biotin: vibrational anharmonicity in the far-infrared. *Chem. Phys. Lett.* **385**, 45–51 (2004).
19. Day, G. M., Zeitler, J. A., Jones, W., Rades, T. & Taday, P. F. Understanding the influence of polymorphism on phonon spectra: lattice dynamics calculations and terahertz spectroscopy of carbamazepine. *J. Phys. Chem. B* **110**, 447–456 (2006).
20. Williams, M. R. C. et al. Terahertz spectroscopy of enantiopure and racemic polycrystalline valine. *Phys. Chem. Chem. Phys.* **13**, 11719–11730 (2011).
21. Choi, W. J. et al. Terahertz circular dichroism spectroscopy of biomaterials enabled by kirigami polarization modulators. *Nat. Mater.* **18**, 820–826 (2019).
22. Dhillon, S. S. et al. The 2017 terahertz science and technology roadmap. *J. Phys. D* **50**, 043001 (2017).
23. Hu, M. et al. Terahertz, infrared and Raman absorption spectra of tyrosine enantiomers and racemic compound. *Spectrochim. Acta A* **254**, 119611 (2021).
24. Liu, Y., Zhou, T. & Cao, J.-C. Terahertz spectral of enantiomers and racemic amino acids by time-domain-spectroscopy technology. *Infrared Phys. Technol.* **96**, 17–21 (2019).
25. True, A. B., Schroeck, K., French, T. A. & Schmuttenmaer, C. A. Terahertz spectroscopy of histidine enantiomers and polymorphs. *J. Infrared Milli. Terahz. Waves* **32**, 691–698 (2011).
26. Shen, Y.-C. Terahertz pulsed spectroscopy and imaging for pharmaceutical applications: a review. *Int. J. Pharm.* **417**, 48–60 (2011).
27. Zeitler, J. A. et al. Terahertz pulsed spectroscopy and imaging in pharmaceutical setting—a review. *J. Pharm. Pharmacol.* **59**, 209–223 (2007).
28. Woutersen, S. et al. Peptide conformational heterogeneity revealed from nonlinear vibrational spectroscopy and molecular-dynamics simulations. *J. Chem. Phys.* **117**, 6833–6840 (2002).
29. Rahman, A., Rahman, A. K. & Rao, B. Early detection of skin cancer via terahertz spectral profiling and 3D imaging. *Biosens. Bioelectron.* **82**, 64–70 (2016).
30. Fitzgerald, A. J. et al. An introduction to medical imaging with coherent terahertz frequency radiation. *Phys. Med. Biol.* **47**, R67 (2002).
31. Jeong, H. H. et al. Dispersion and shape engineered plasmonic nanosensors. *Nat. Commun.* **7**, 11331 (2016).
32. Grimme, S., Bannwarth, C. & Shushkov, P. A robust and accurate tight-binding quantum chemical method for structures, vibrational frequencies, and noncovalent interactions of large molecular systems parametrized for all *spd*-block elements ($Z=1$–86). *J. Chem. Theory Comput.* **13**, 1989–2009 (2017).
33. Kim, Y. et al. Reconfigurable chiroptical nanocomposites with chirality transfer from the macro- to the nanoscale. *Nat. Mater.* **15**, 461–468 (2016).
34. Provenzano, C., Pagliusi, P., Mazzulla, A. & Cipparrone, G. Method for artifact-free circular dichroism measurements based on polarization grating. *Opt. Lett.* **35**, 1822–1824 (2010).
35. Ruggiero, M. T., Sibik, J., Orlando, R., Zeitler, J. A. & Korter, T. M. Measuring the elasticity of poly-L-proline helices with terahertz spectroscopy. *Angew. Chem. Int. Ed.* **55**, 6877–6881 (2016).
36. Wukovitz, S. W. & Yeates, T. Why protein crystals favour some space-groups over others. *Nat. Struct. Biol.* **2**, 1062–1067 (1995).
37. Jepsen, P. U. & Fischer, B. M. Dynamic range in terahertz time-domain transmission and reflection spectroscopy. *Opt. Lett.* **30**, 29–31 (2005).
38. Yin, X., Schäferling, M., Metzger, B. & Giessen, H. Interpreting chiral nanophotonic spectra: the plasmonic Born–Kuhn model. *Nano Lett.* **13**, 6238–6243 (2013).
39. Sala, J., Guàrdia, E. & Masia, M. The polarizable point dipoles method with electrostatic damping: implementation on a model system. *J. Chem. Phys.* **133**, 234101 (2010).
40. Dos Santos, L. H. R., Krawczuk, A. & Macchi, P. Distributed atomic polarizabilities of amino acids and their hydrogen-bonded aggregates. *J. Phys. Chem. A* **119**, 3285–3298 (2015).
41. Kühne, T. D. et al. CP2K: an electronic structure and molecular dynamics software package—Quickstep: efficient and accurate electronic structure calculations. *J. Chem. Phys.* **152**, 194103 (2020).
42. Davies, C. L., Patel, J. B., Xia, C. Q., Herz, L. M. & Johnston, M. B. Temperature-dependent refractive index of quartz at terahertz frequencies. *J. Infrared Milli. Terahz. Waves* **39**, 1236–1248 (2018).
43. Xie, L. et al. Temperature-dependent terahertz vibrational spectra of tetracycline and its degradation products. *Spectrochim. Acta A* **222**, 117179 (2019).
44. Altfeder, I. et al. Scanning tunneling microscopy observation of phonon condensate. *Sci. Rep.* **7**, 43214 (2017).
45. Lundholm, I. V. et al. Terahertz radiation induces non-thermal structural changes associated with Fröhlich condensation in a protein crystal. *Struct. Dyn.* **2**, 054702 (2015).
46. Rimer, J. D. et al. Crystal growth inhibitors for the stones through molecular design. *Science* **330**, 337–341 (2010).
47. Kawase, M. et al. Application of terahertz absorption spectroscopy to evaluation of aging variation of medicine. *Anal. Sci.* **27**, 209–212 (2011).
48. Ow, S. Y. & Dunstan, D. E. A brief overview of amyloids and Alzheimer's disease. *Protein Sci.* **23**, 1315–1331 (2014).
49. Ivanova, M. I., Sievers, S. A., Sawaya, M. R., Wall, J. S. & Eisenberg, D. Molecular basis for insulin fibril assembly. *Proc. Natl Acad. Sci. USA* **106**, 18990–18995 (2009).
50. Jiménez, J. L. et al. The protofilament structure of insulin amyloid fibrils. *Proc. Natl Acad. Sci. USA* **99**, 9196–9201 (2002).

Methods

Materials. Unless otherwise noted, all the reagents were purchased from Sigma-Aldrich and Tokyo Chemical Industry and used as received without further purification.

Recrystallization of AAs and preparation of other samples. A recrystallization process is described by a flow diagram in Supplementary Fig. 1. In general, samples (approximately 0.5–2.0 g) of AA enantiomers were stirred in a glass vial in boiling E-pure water until completely dissolved. The resultant hot solution was transferred into a Petri dish covered with a lid and left undisturbed for ~1 day for the crystal growth. The obtained crystals were carefully filtered and washed with ethanol at least three times under reduced pressure. For anhydrous crystals, the filtered crystals were further dried at 60 °C under a reduced pressure for at least 12 h.

Specific recrystallization conditions for AAs are summarized in Supplementary Table 1. E-pure water was used as a solvent for most AAs, whereas 1 M oxalic acid solution and ethanol were used for Tyr and proline (Pro), respectively, due to their low solubility in E-pure water. The hydration states of arginine (Arg) and asparagine (Asn) were controlled by the final heat-drying process; as-recrystallized hydrated forms of arginine and asparagine crystals can be converted, by heat drying at 60 °C, into their anhydrous forms. Lysine (Lys) was used as received without further recrystallization.

Detailed preparation of other samples including dipeptide, amyloid fibrils of insulin and cystine stones are described in the Supplementary Information.

Characterization of crystalline phases and sizes of crystals. Crystalline phases of crystals were characterized by PXRD measurements using a SmartLab powder X-ray diffractometer (Rigaku) equipped with a 2.2 kW Cu anode (Cu Kα; wavelength, $\lambda = 1.54$ Å), a Kβ filter and a D/teX Ultra 250 high-speed silicon strip one-dimensional detector. The PXRD data were collected in the range of 15–60° in 2θ by the step-scan mode with a step size of 0.01°. The crystals were ground using a pestle and mortar and mounted onto a glass plate for their PXRD measurements. The phase purity and space group of the crystals were analysed by comparing their experimental diffraction patterns with the reported data of the corresponding single crystals. The single-crystal data were collected from the Cambridge Crystallographic Data Centre and their diffraction patterns were reproduced using the Mercury software. Supplementary Figs. 2 and 3 show the PXRD patterns of crystals, and their crystalline phases are summarized in Supplementary Table 2.

Scanning transmission imaging was performed using scanning transmission electron microscope detector equipped in the Thermo Fisher Helios 650 Nanolab scanning electron microscopy (SEM)/FIB instrument (Supplementary Fig. 5). The crystal powders were dispersed on copper TEM grids with an ultrathin carbon film on a lacey carbon support purchased from Ted Pella. Specimens of the TEM grid were loaded on a TEM grid holder and the images were taken using an electron gun with an acceleration voltage of 29 kV and current of 0.4 nA. Three different detector modes of secondary electron and high-angle annular dark and bright fields were simultaneously used for the same sample to obtain information about the morphology.

The precise size and crystal habit of each AA crystal was measured and observed by an SEM instrument (TESCAN MIRA3 FEG SEM) (Supplementary Fig. 4), respectively. Their size distributions were also estimated by static light-scattering measurements using a Mastersizer 2000 (Malvern) equipped with a Hydro 2000S wet dispersion unit.

Preparation of slurry samples. The use of slurry samples has long been adopted in infrared spectroscopy, known as the Nujol mull method. Slurry samples of powders, 50 wt%, were prepared by mixing ~150 mg of ground crystals with ~150 mg (~180 µl) MO using a micro-spatula. The slurry samples were placed between two quartz plates with a ~100-µm-thick spacer, and the sandwich cell was pressed by clamps to ensure a flat surface without voids.

THz-TDP setup. THz-TDP was used to measure the chiroptical responses of the AA samples. The generation and detection of the THz waveform were accomplished with a standard time-domain THz spectrometer (TeraSmart, Menlo Systems) using photoconductive antennas with a pulsed laser at 1,560 nm. The same TERA15-FC antenna modules were used as the emitter and detector. Four identical lenses (TPX50, Menlo Systems) made of TPX polymer (polymethylpentene) with a diameter of 38.1 mm and a focal length of 50 mm were used to make collimated THz rays.

Temperature-dependent THz-TDP measurements of the samples were performed using a metal–ceramic heater (HT19R, Thorlabs). The heating temperature was finely controlled by a power supply and the temperature range of 296–456 K was achieved with a temperature stability of ±1 K.

Sample scanning in the THz focal plane was achieved by a motorized X–Y stage. Three linear polarizers were used to determine the optical rotatory dispersion (TORD, θ) and circular dichroism (TCD, η) of arbitrarily polarized THz waves. Here micropatterned gold strips on the parylene C film were used for wire-grid polarizers exhibiting a high extinction ratio over the THz range. More detailed results are provided in the Supplementary Discussion (Supplementary Fig. 12).

Density functional theory calculations for crystalline AA or dipeptide supercell. The AA or dipeptide unit cell was replicated along the *a*, *b* and/or *c* directions to draw the supercell model systems with edge lengths of at least 1 nm. Energy minimization was performed for each system by relaxing both molecular geometries and cell vectors but enforcing the shape corresponding to the corresponding space group. The pressure tolerance was set to 10 bar and an external pressure of 1 bar was applied to the diagonal elements. Following the geometry optimization and vibrational analysis procedures, a short molecular dynamics (MD) equilibration run was performed at the *NVT* ensemble (1 ps, temperature $T = 300$ K) using the canonical sampling through velocity rescale thermostat with a 5 fs time constant (strong coupling). The final coordinates and velocities were taken as an input for a longer MD production run (50 ps, *NpT* ensemble, $T = 300$ K using the Nosè–Hoover thermostat with coupling constant $\tau_T = 100$ fs and pressure $p = 1$ bar with anisotropic coupling at fixed symmetry with coupling constant $\tau_p = 1$ ps). Coordinates, velocities and Löwdin charges were saved for all the timesteps of the production runs to compute the TA and TCD data.

Data availability

The data that support the plots within this paper and other findings of this study are available from the corresponding authors upon reasonable request.

Code availability

The analysis codes that support the findings of this study are available from the corresponding authors upon reasonable request.

Acknowledgements

This work was supported by Vannevar Bush DoD Fellowship to N.A.K. titled 'Engineered Chiral Ceramics' ONR N000141812876, ONR COVID-19 Newton Award 'Pathways to Complexity with "Imperfect" Nanoparticles' HQ00342010033. This study was also supported in part by the US Defense Advanced Research Projects Agency (DARPA) RadioBio programme under contract HR00111720067, by the Office of Naval Research (MURI N00014-20-1-2479) and by AFOSR FA9550-20-1-0265. Additionally, the computational part of this work was supported by the Brazilian funding agencies CAPES (finance code 001), CNPq (311353/2019-3) and FAPESP (processes 2012/15147-4 and 2013/07296-2), and the high-performance computer resources provided by the SDumont supercomputer at the National Laboratory for Scientific Computing (LNCC/MCTI, Brazil) and Cloud@UFSCar. We acknowledge the Cambridge Crystallographic Data Centre for the collection of single-crystal data and use of the Mercury software. K.Y. thanks the Japan Society for the Promotion of Science for a JSPS Young Scientist Fellowship and the Overseas Research Program of the Yoshida Foundation for Science and Technology. We also acknowledge the financial support of the University of Michigan College of Engineering and NSF grant no. DMR-0723032, as well as technical support from the Michigan Center for Materials Characterization.

Author contributions

W.J.C. and N.A.K. designed the project. K.Y. recrystallized the AAs and dipeptides and conducted the PXRD analysis and size distribution analysis. J.-Y.K., W.J.C. and K.S. conducted the SEM and TEM imaging. W.J.C. measured all the THz spectra and developed the algorithm for TA, TCD and TORD. Dynamic time-warping, correlation matrix and violin plots were performed by M.C. W.J.C. and S.H.L. developed the algorithm for the BK theory and S.H.L. conducted the parametric fitting using the nonlinear regression method. F.M.C. and A.F.d.M. conducted the density functional theory simulation and analysed the data. Y.W. performed the MD simulation. J.M.K. removed the cystine stones in clinical purpose and provided them as samples. All the authors discussed the results. W.J.C., A.F.d.M. and N.A.K. wrote the manuscript.

Competing interests

The authors declare no competing interests.

Additional information

Supplementary information The online version contains supplementary material available at https://doi.org/10.1038/s41566-022-00969-1.

Correspondence and requests for materials should be addressed to André F. de Moura or Nicholas A. Kotov.

Peer review information *Nature Photonics* thanks the anonymous reviewers for their contribution to the peer review of this work.